

# Imaging performance of a prototype scanned-slot digital mammography system

Andrew D.A. Maidment, Martin J. Yaffe, Donald B. Plewes,  
Gordon E. Mawdsley, Ian C. Soutar, and Brian G. Starkoski.

Departments of Medical Biophysics and Radiology, University of Toronto,  
and Research Division, Sunnybrook Health Science Centre,  
2075 Bayview Avenue, Toronto, Ontario M4N 3M5

## ABSTRACT

A prototype of a clinical scanned-slot digital mammography imaging system has been developed, which demonstrates better contrast sensitivity and latitude than current state-of-the-art film-screen mammography systems. The detector consists of a  $\text{Gd}_2\text{O}_2\text{S:Tb}$  phosphor screen coupled via a 2-to-1 demagnifying fiber-optic taper to two time-delay integration (TDI) charge-coupled device (CCD) image arrays. Images are obtained by scanning the 4.0 mm wide by 21 cm long detector across the image field. An 18 cm by 21 cm image contains 2900 by 4032 pixels, of dimension  $62 \mu\text{m} \times 52 \mu\text{m}$  at the detector. Currently, images are produced in 7.8 seconds using a 40 kV tungsten-target spectrum with a total heat load of 50 kJ, giving a mean glandular dose of 0.85 mGy (85 mrad) to a 5 cm thick 50% glandular, 50% adipose breast. The detector has a limiting resolution of 9.5 lp/mm. A clinical version of this prototype, which incorporates several improvements, is being constructed.

## 1. INTRODUCTION

Film-screen mammography is currently the most sensitive modality for the early detection of breast cancer<sup>1,2,3</sup>. However, the detection of subtle lesions using film-screen imaging systems is limited by insufficient latitude, film granularity noise, and dose-inefficient scatter rejection<sup>4</sup>. The range of exposures present at the exit surface of the compressed female breast exceeds the range over which the display contrast gradient of mammographic film-screen combinations is near maximum<sup>4,5</sup>. As a result, highly attenuating and highly transmissive regions of the breast are often imaged with sub-optimal contrast. In these regions, film granularity noise is nearly equal to x-ray quantum noise even at zero spatial-frequency<sup>6</sup>. At high spatial-frequencies, the magnitude of film granularity noise exceeds that of x-ray quantum noise<sup>6,7</sup>. Finally, radiation scattered by the breast and incident upon the image receptor reduces contrast<sup>8</sup> and contributes to image noise. Current scatter rejection methods are relatively effective, but they necessitate a 90 to 150% increase in dose<sup>9</sup>.

The technical limitations of film-screen mammography arise in part because the film must serve in multiple roles: as the detector, the image display device, and the image storage device. We have demonstrated<sup>4,10</sup> that these technical limitations can be overcome with a digital mammography imaging system because image acquisition, display and storage are performed independently, so that each process can be optimized separately.

A detector for digital mammography must be capable of imaging all regions of a breast with adequate contrast and must ensure that all regions of the image are x-ray quantum-noise-limited. Ideally, a digital detector exhibits a linear response over a wide range of exposures and has little inherent noise. Appropriate image contrast in any region of the breast can be obtained after image acquisition by altering the display contrast. X-ray quantum-noise-limited images can be obtained by removing the effects of temporally invariant fixed-pattern "noise".

We have chosen to remove scattered radiation by scanning geometrically-aligned pre- and post-patient collimators across the breast during image acquisition. This method allows almost complete removal of scatter with little or no attenuation of primary x-ray quanta<sup>11,12,13</sup>, providing a more dose-efficient means of scatter removal than radiographic grids which attenuate a fraction of the primary radiation. In film-screen mammography, optimal contrast is obtained at a specific exposure. If scattered radiation is removed from the beam, its energy must be replaced by increasing the dose to the breast. In a digital system with sufficient dynamic range, the detector exposure is determined by the signal-to-noise ratio requirements. In this paper, we describe the design and the preliminary performance analysis of a scanned-slot digital mammographic imaging system.

## 2. SYSTEM DESCRIPTION

### 2.1. Mechanical Design

The scanned-slot digital mammography prototype under development in our laboratory is shown schematically in Figure 1. The system is built upon a swing-arm which is mounted to a conventional mammography gantry. At one end of the swing-arm is the x-ray tube; at the other is the detector. The arm is mounted such that the x-ray tube pivots about the focal spot, and the 4.0 mm wide, 21.0 cm long detector is swung in an arc from the chest wall to the nipple in a continuous motion. The detector has been designed to minimize the amount of breast tissue near the patient's chest wall which can not be imaged. By pivoting the x-ray tube, the angle between the target of the x-ray tube and the detector is independent of scan position, thereby avoiding variations in x-ray fluence due to the heel effect. More importantly, the constant angle provides an effective focal spot size that is invariant with scan position.

Two slot-shaped collimators are scanned with the detector. One is mounted on the x-ray tube to restrict the region of irradiation to a narrow slot, while the second is mounted near the detector to remove scattered radiation. Using a 250 cm<sup>2</sup>, 6 cm thick phantom composed of the breast equivalent plastic, BR12, and a 4.0 mm slot width, we measured a scatter-to-primary ratio of 0.05 - less than one half of that achieved with a mammographic grid.

A tungsten target angiographic x-ray tube (GE-CGR, RSN 776) is currently used to provide a 0.3 mm nominal focal spot size with a 16 kW power rating. A high frequency x-ray generator (Varian, HF650) was modified by the manufacturer to produce stable outputs at low kilovoltages. All images and tests were performed at 40 kV (HVL of 0.95 mm Al), with a tube current of 160 mA (8.9 mR/mAs at 60 cm), a scanning speed of 2.3 cm s<sup>-1</sup> (measured at the detector input), and a 60 cm source-image distance (SID). Currently, a total scan time of 7.8 seconds is required to produce an 18 cm long image. The mean glandular dose to a 5 cm thick, 50% adipose, 50% glandular breast is 0.85 mGy using this technique. We have shown previously<sup>14</sup> that use of a more penetrating x-ray beam than that employed in conventional mammography offsets, in part, the inefficiency of x-ray tube heat loading inherent in a scanned system, without unduly reducing the signal-to-noise ratio.

### 2.2. Detector Design

The detector, shown in Figure 2, consists of a phosphor material coupled via two fiber-optic (FO) tapers to two time-delay integration (TDI) mode charge-coupled device (CCD) image arrays. A 31.7 g cm<sup>-2</sup> Gd<sub>2</sub>O<sub>2</sub>S:Tb phosphor screen<sup>15</sup> is used to convert x rays to light. The FO tapers provide a 2:1 demagnification. Each CCD has a format of 64 x 2048 square pixels of size 27 μm (yielding pixels of dimension 50 μm in the midplane of the breast). Because of an overlap at the junction of the CCDs, the image has a width of 4032 pixels. The length of the image is dependent upon the distance scanned. For example, an 18 cm scan produces 2900 lines of data.

A TDI CCD operates in a manner which allows images to be acquired while continuously moving the detector across the breast. The detector is moved past the object at a constant speed, while the charge collected in each CCD element is shifted in the opposite direction at the same speed. In this way, the charge corresponding to the signal from a given image pixel is integrated as it is shifted across the CCD. Since the digital image is stationary with respect to the transmitted x-ray pattern

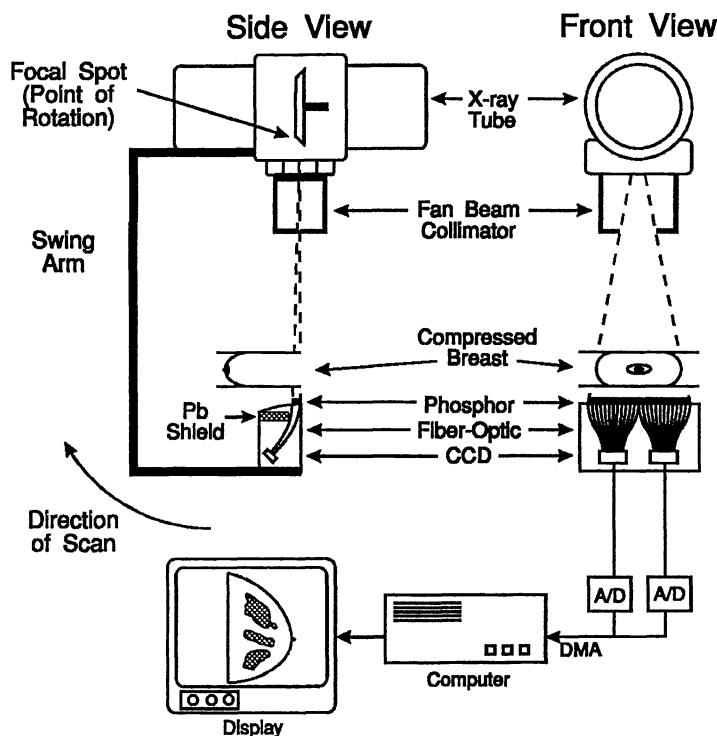


**Figure 1** Schematic of the prototype digital mammography system in two projections. The x-ray tube and detector are mounted on a swing arm that pivots about the focal spot of the x-ray tube.

produced by the breast, a narrow detector can be scanned in continuous motion past a large object to produce an arbitrarily large image.

Each CCD image array has 16 parallel output-channels for rapid data acquisition. Each channel has a separate DC offset, amplifier, and analog-to-digital converter (A/D). The CCD output signal consists of a small image signal (less than 200 mV) and a large 5 volt offset. The offset for each output-channel is removed by subtraction of a reference voltage which is varied under computer control by digital-to-analog converters. This method allows for fine adjustment of the reference voltage which is varied under computer control by digital-to-analog converters. The image signal is then amplified by a factor of approximately 50. The ADCs each operate at a maximum conversion rate of  $2.0 \times 10^5$  samples per second. The digital data from the 32 ADCs are multiplexed and transferred to an IBM-compatible 486-based computer using a direct memory access (DMA) interface card containing a 32 megabyte dual-port image memory. The maximum data transfer rate is 1150 lines per second (10 megabytes/sec). Therefore, in principle a  $21 \times 18 \text{ cm}^2$  mammogram could be acquired in 2.5 seconds.

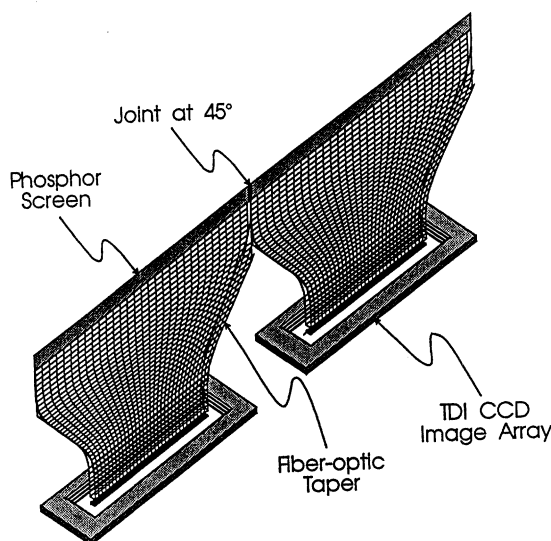


**Figure 2** Schematic of the detector showing the phosphor coupled via 2:1 demagnifying fiber-optic tapers to two CCD image arrays. The junction between the tapers is angled at  $45^\circ$  to the scanning motion.

To accommodate images spanning the full width of the breast, two or more CCD image arrays are required. To prevent data loss at the junctions of the CCD arrays, the ends of the FO tapers were milled at a  $45^\circ$  angle. Hence, the image fields on the two TDI CCDs overlap at the input of the detector and, as a result, data in the overlap region are not lost. In this paper, all images were acquired with a single CCD.

### 3. SYSTEM CHARACTERIZATION

#### 3.1. Linearity

The linearity of the response of the detector to x rays was measured by varying the beam current of the x-ray tube from 2 to 160 mA, and by varying the SID by a factor of 4. The data acquired at the two SIDs were combined using a bootstrap technique. The result was a 1260-fold variation in the detector exposure. The response of the CCD,  $S$ , as a function of radiant intensity,  $I$ , was fitted to a power relationship,

$$S = kI^\gamma \quad (1)$$

where  $k$  and  $\gamma$  are fitted parameters. The least squares fit is  $\gamma = 0.99 \pm 0.01$ , and  $k = 5.05 \pm 0.01 \text{ ADU mR}^{-1}$ . The measured and fitted data are shown in Figure 3.

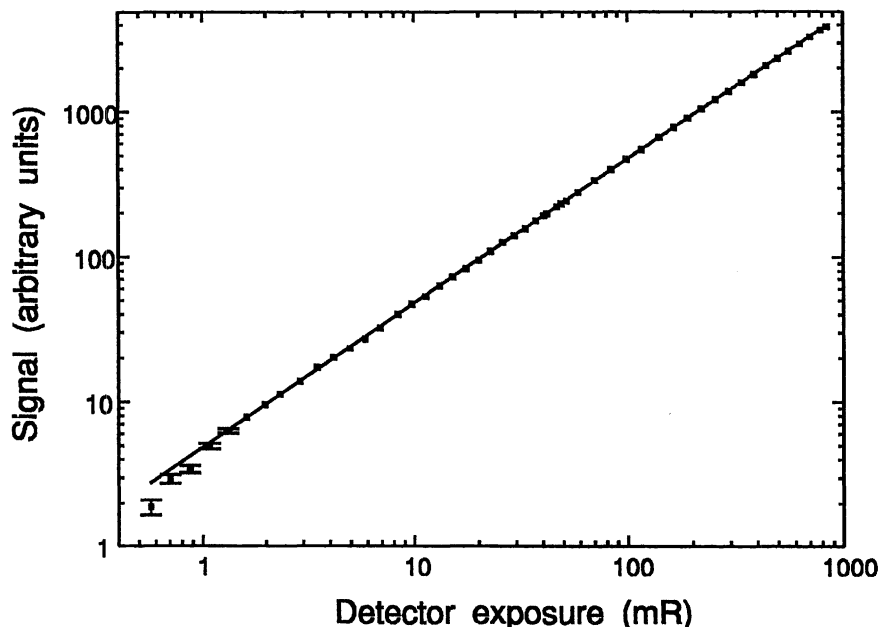


**Figure 3** Measured response of the detector to incident x-ray exposure. Also shown is the least squares fit of the data to Equation 1.

### 3.2. Quantum Accounting

The number of quanta at various points in the detector system has been determined, and the results of this "quantum accounting" are shown in Figure 4. The x-ray quantum fluence, the quantum detective efficiency (QDE) of the phosphor screen, and the number of light quanta produced per x-ray interaction were calculated using a method described previously<sup>14,16</sup>. This method accounts for the energy dependence of the x-ray spectra, attenuation, and light production. Assuming a 40 kV W-target spectrum (1.0 mm Al HVL), 230 x rays are incident per pixel per mR (stage A), and the QDE is 49%. The number of x rays interacting is shown in stage B. On average 800 light quanta are produced per x-ray interaction (stage C). The NA of the FO taper is 0.6 and the fractional active area is 0.8, therefore only 29% of the light from stage C is incident within the acceptance solid angle of the FO (stage D). We have measured that the current FO taper provides a 4.4 fold reduction in pixel area (i.e. 62  $\mu\text{m}$  x 52  $\mu\text{m}$  pixels at the phosphor, 27  $\mu\text{m}$  x 27  $\mu\text{m}$  pixels at the CCD), which reduces the light output of the FO taper by a similar amount (stage E). In this prototype detector, the CCD has a separate FO window which has a light transmission efficiency of 57% (stage F). Thus 30 light quanta per x-ray interaction are incident upon the CCD.

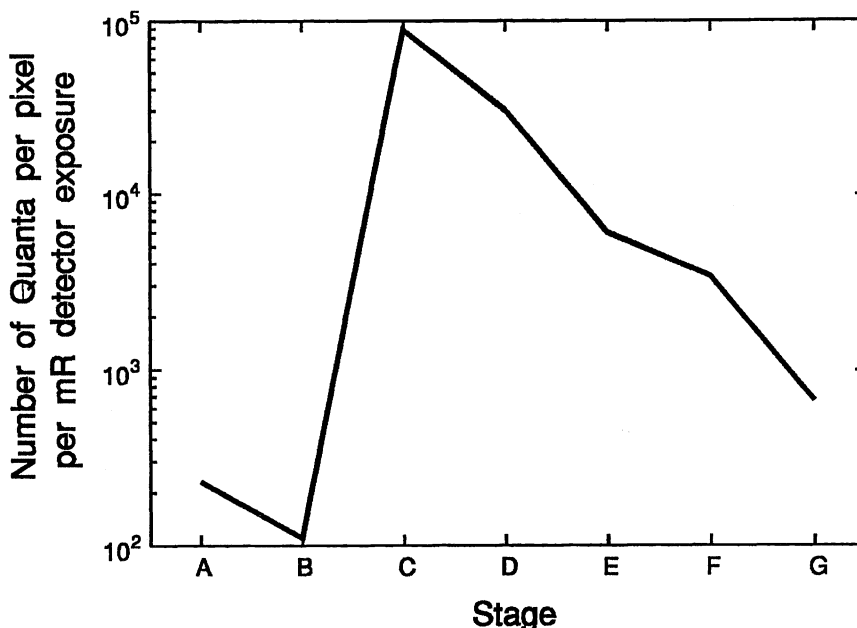


**Figure 4** Quantum accounting, showing the number of quanta at each stage in the imaging system. Stages A-G are described in the accompanying text.

The optical quantum detection efficiency of the CCD was calculated by weighting the response of the CCD<sup>17</sup> with the spectrum of the light produced by the screen<sup>18</sup> using the method of Eberhardt<sup>19,20</sup>. The effective optical quantum detection efficiency of the CCD is 20% (stage G). Thus, 6.1 electrons are produced in the CCD per x-ray absorbed in the phosphor. This value is sufficient to ensure that the detector is x-ray quantum-noise-limited at zero spatial-frequency.

The output signal of the CCD image array was quantified using the mean-variance technique<sup>21,22</sup>, whereby the mean and variance of the CCD response are measured parametrically as a function of illumination. For a detector where the generation of signal carriers (i.e. electrons) is governed by Poisson statistics and where the variance in the detector gain is small, it can be shown that

$$\sigma_s^2 = \bar{G} \bar{S} + \sigma_{dark}^2 \quad , \quad (2)$$

where  $\bar{G}$  is the mean conversion gain of the detector in analog-to-digital conversion units (ADU) per signal carrier,  $\bar{S}$  is the observed mean signal in ADU,  $\sigma_s^2$  is the observed variance in ADU<sup>2</sup>, and  $\sigma_{dark}^2$  is the variance due to signal-independent or "dark" noise. A linear least squares fit of data to Equation 2 gave  $\bar{G} = 0.0076 \pm 0.0001$  ADU electron<sup>-1</sup> (i.e. 132  $\pm$  2 electrons per ADU) and  $\sigma_{dark} = 3.0 \pm 0.1$  ADU (i.e. 396  $\pm$  15 electrons). From the known amplifier gain and ADC calibration, we calculated that the output sensitivity of the CCD is 0.37  $\mu\text{V}$ /electron. The output sensitivity of this type of CCD was measured previously by Hguyen, *et al.*<sup>23</sup> to be 1.1  $\mu\text{V}$ /electron. The reason for the discrepancy between their result and the results presented in this paper is being investigated.

### 3.3. Resolution

The modulation transfer function (MTF) of the imaging system was measured using a slanted-edge technique<sup>24,25</sup>. In this method, a 0.4 mm thick tantalum blade was scanned across the detector in synchrony with the TDI charge transfer. The blade was placed at about a 2° angle to either the columns or the rows of the CCD. The results are shown in Figure 5. The MTF was calculated both in the direction of the scanning motion (labelled "Scan"), and perpendicular to the scan direction (labelled "Slot"). The MTF of a Kodak Min-R Medium, OM-1 screen-film combination<sup>26</sup> is shown for comparison. The spatial frequency at which the value of MTF decreased to 0.05 is 8.7 mm<sup>-1</sup> in the slot direction, and 5.7 mm<sup>-1</sup> in the scan direction. The current FO taper is anisotropic (i.e. the demagnification is different in the two directions), hence the sampling frequencies differ, being 9.6 mm<sup>-1</sup> in the slot direction and 8.1 mm<sup>-1</sup> in the scan direction.

The limiting resolution of the detector was measured with a Pb star pattern. Limiting resolutions of 8.5 and 5.3 lp/mm were measured in the slot and scan directions, respectively, which are close to the measured 5% values of the MTF. By employing digital unsharp masking, the observed limiting resolution was significantly improved. An image of a Pb star pattern acquired at a 45° angle to the scanning motion is shown in Figure 6 after unsharp masking. The limiting resolution is about 9.5 lp/mm, which is equal to the sampling frequency. We believe that digital filtering improved the observed resolution by reducing the effect of 1/f noise (described below). Note that vertical linear dislocations occur in 3 places in the image. These dislocations are the result of manufacturing flaws in the FO taper. Gross dislocations in the image are currently corrected with a computer algorithm which moves each vertical line in Figure 6 an integral number of pixels up or down for accurate alignment. Currently, variations of less than a pixel are not corrected. Improvements in the FO taper manufacture should reduce or eliminate the need for these corrections.

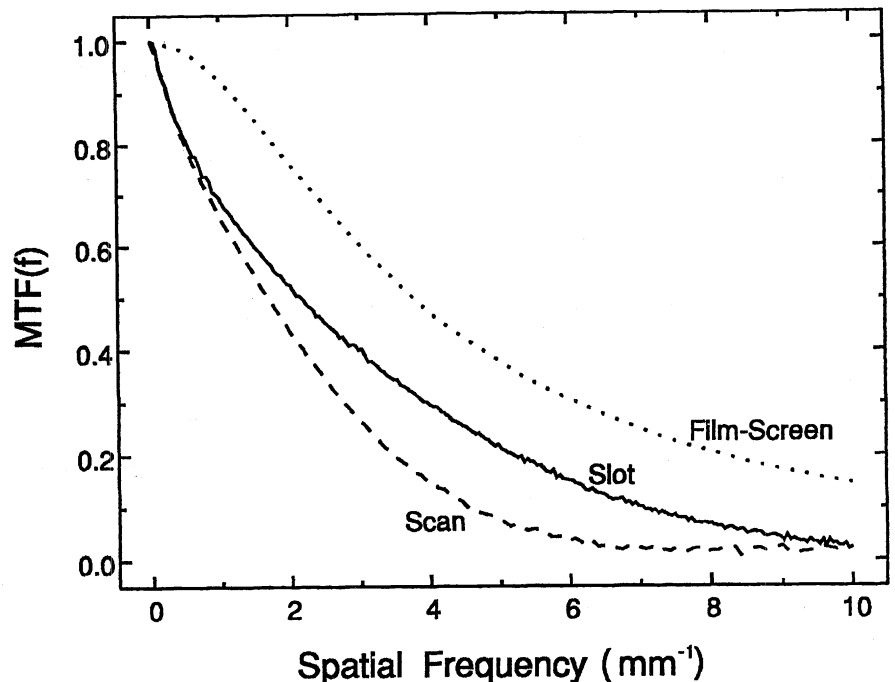


Figure 5 The detector MTF in the direction parallel to ("Scan") and perpendicular to ("Slot") the scanning motion, and, the MTF of a Kodak Min-R medium, OM-1 screen-film combination.

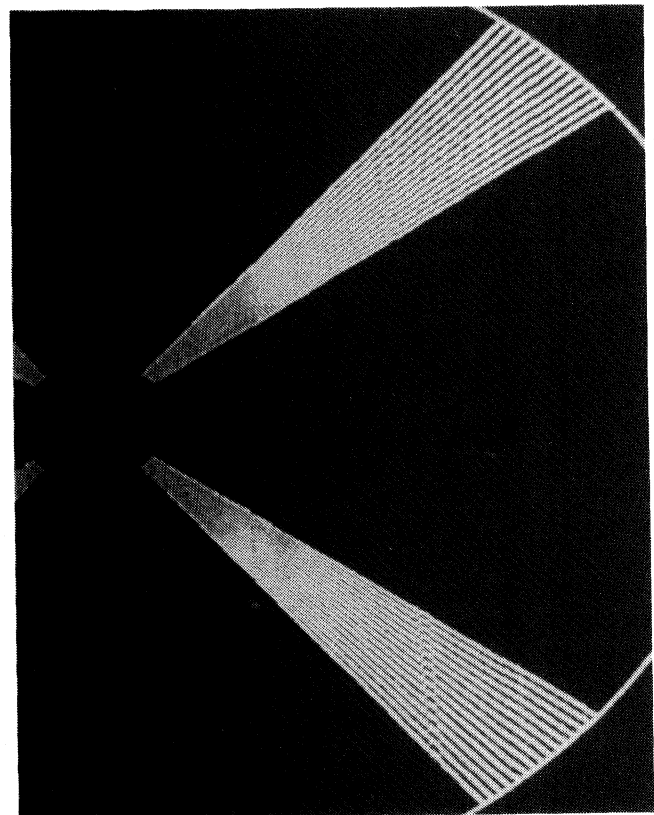


Figure 6 Image of a 0.5°, 45 mm diameter, Pb-star pattern. The image is displayed after unsharp masking. A limiting resolution of 9.5 lp/mm is seen.

### 3.3.1. Slot direction

The MTF in the slot direction was compared to theoretical results based on the aperture response of the CCD and the MTF of the screen, as shown in Figure 7-a. Plotted, are the aperture response ( $MTF_{ap}$ ), the MTF of the phosphor screen<sup>26</sup> ( $MTF_s$ ), the experimentally measured MTF ( $MTF_{exp}$ ), and  $MTF_{oc}$  [given by the ratio,  $MTF_{exp}/(MTF_{ap} MTF_s)$ ]. All MTFs are expressed in terms of spatial frequencies measured at the plane of the phosphor screen.

The MTF at a spatial frequency,  $f$ , due to the size and shape of the pixel is given by

$$MTF_{ap} = \text{sinc}(f \Delta x) \quad , \quad (3)$$

where  $\Delta x$  is the pixel size in the slot direction, and  $\text{sinc}(x) = \sin(\pi x)/(\pi x)$ .

We believe that  $MTF_{oc}$  is due to blurring which occurs in the optical coupling between the phosphor screen and the CCD detector elements. The CCD FO window, the FO taper, and the coupling compounds used between each component contribute to  $MTF_{oc}$ . Note that  $MTF_{oc}$  undergoes a significant low frequency drop ( $MTF_{oc} = 0.7$  at  $1.5 \text{ mm}^{-1}$ ). This is the result of veiling glare, due both to multiple reflections within the coupling media, and to cross-talk between optical fibers. These problems can be addressed by using higher quality fiber-optics (which are available), and by mounting the FO taper directly on the CCD to reduce the number of points of coupling between the phosphor screen and the CCD. As an added benefit, the direct mounting of the taper to the CCD would increase the overall coupling efficiency by a factor of 2. Further evaluation of  $MTF_{oc}$  is required.

### 3.3.2. Scan direction

The MTF in the scan direction was compared to theoretical results based on the aperture response of the CCD pixel and the spatial and temporal response of the screen, as shown in Figure 7-b. Plotted, are the aperture response ( $MTF_{ap}$ ), the effect of the 4-phase clock structure ( $MTF_\phi$ ), the effect of the temporal response of the phosphor material ( $MTF_{lag}$ ), the MTF of the phosphor screen ( $MTF_s$ ), the MTF of the optics ( $MTF_{oc}$ ), the product of these factors ( $MTF_{th}$ ), and the experimentally measured MTF ( $MTF_{exp}$ ). Again, all spatial frequencies are expressed in the plane of the phosphor.  $MTF_{oc}$  is assumed to be the same in the scan and slot directions. Similarly, the spatial resolution of the phosphor screen is assumed to be isotropic.

In the scanning direction, the discrete motion of the charge packets due to the finite number of clock phases per pixel increases the effective size of the pixel in the scan direction. The degradation in the MTF at a spatial frequency,  $f$ , due to the clock structure is given by<sup>27</sup>

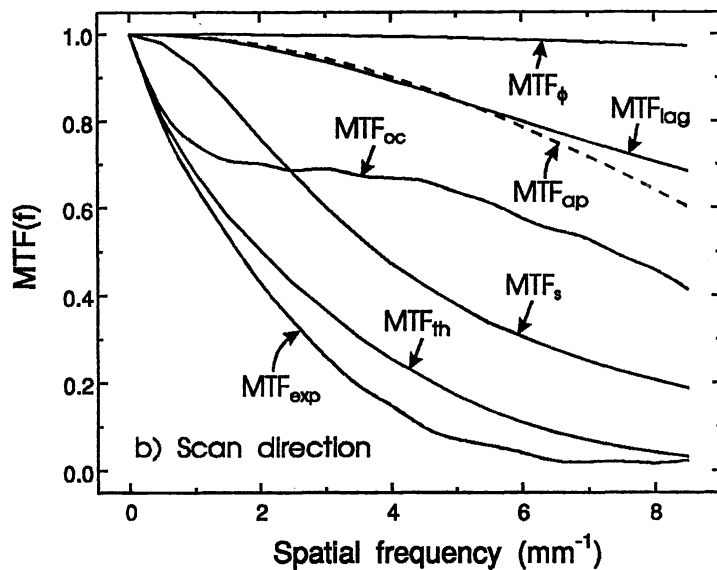
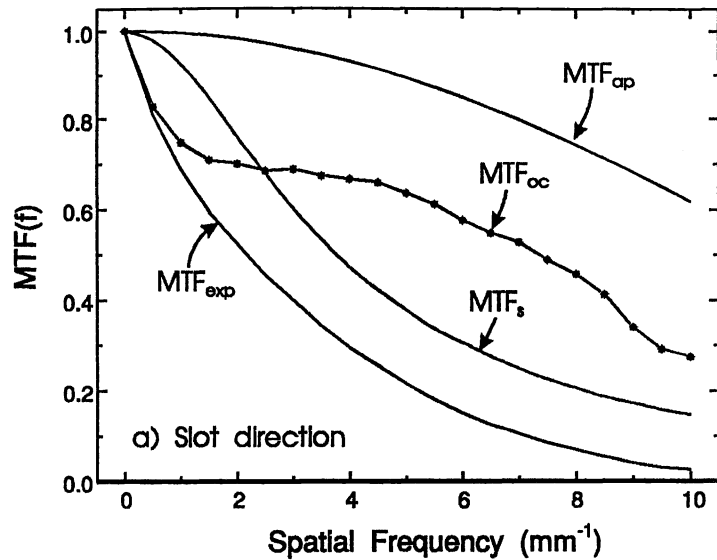


**Figure 7** The measured MTF in a) slot and b) scan direction. Calculated constituent MTFs are shown, accounting for pixel size, screen spatial and temporal response, and optics.

$$MTF_{\phi}(f) = \text{sinc}\left(\frac{f \Delta y}{n}\right), \quad (4)$$

where  $\Delta y$  is the pixel size in the scan direction, and  $n = 4$  is the number of clock phases per pixel. In our CCD, this results in a 3% drop in MTF at the sampling frequency. The temporal response of the phosphor material (i.e. the lag) results in a blurring of the image in the scan direction. The MTF of the blurring is given by

$$MTF_{lag}(f) = (1 + (2 \pi f/k)^2)^{-1/2}, \quad (5)$$

$$\text{where } k = \ln(2)/(vt_{1/2})$$

assuming the temporal decay of light output from the phosphor screen may be represented by a single exponential. The time for the light output to drop 50% in intensity is given by  $t_{1/2}$ , and the temporal response of the phosphor is related to the spatial response of the detector by the scan speed,  $v$ . For the  $\text{Gd}_2\text{O}_2\text{S:Tb}$  phosphor which we used<sup>28</sup>,  $t_{1/2} = 0.6$  msec.

Note that the experimentally measured  $MTF_{exp}$  is still lower than that predicted by the product of the above factors,  $MTF_{th}$ . We believe that the additional degradation is due to microphonics and variations in the demagnification of the FO taper with position in the CCD.

In all of the MTF measurements, above, the scanning speed was precisely matched to the charge transfer rate. To measure the effect of mismatch between the scan speed and the charge transfer rate, the scan speed of the tantalum edge was varied  $\pm 25\%$  about the optimum. The effect of scan speed on MTF is plotted in Figure 8, where the spatial frequency at which the  $MTF = 0.1$  is shown. The spatial resolution degradation is given by<sup>29</sup>

$$MTF_{\Delta v} = \text{sinc}\left(N \Delta y \frac{\Delta v}{v} f\right), \quad (6)$$

where  $N = 64$  is the number of pixels in the scan direction,  $\Delta y$  is the pixel size,  $v$  is the scanning speed,  $\Delta v$  is the difference between the scan speed and the charge transfer speed, and  $f$  is the spatial frequency. Figure 8 shows good agreement between the experimental data and the theoretical prediction.

### 3.4. Noise

The image data used to calculate the NPS were acquired with the entire detector area uniformly irradiated. The NPS were calculated by employing the direct Fourier transform method<sup>4,30,31</sup>. Data were summed in one direction to synthesize the effect of a scanning slit<sup>4</sup>. To measure the NPS in the scan direction a synthetic slit 62  $\mu\text{m}$  wide and 6.6 mm long was used, while a 52  $\mu\text{m}$  x 7.9 mm synthetic slit was used to measure the NPS in the slot direction. To reduce random error in spectral estimates, the individual power spectra from 12 images were averaged. The image format allowed 8 synthesized slots to be obtained per image. Each synthesized record contained 1024 elements. Corrections for the finite length and width of the synthetic aperture allowed the true noise power spectrum to be estimated. In this way, estimates of the two orthogonal central sections of the 2-D NPS are obtained.

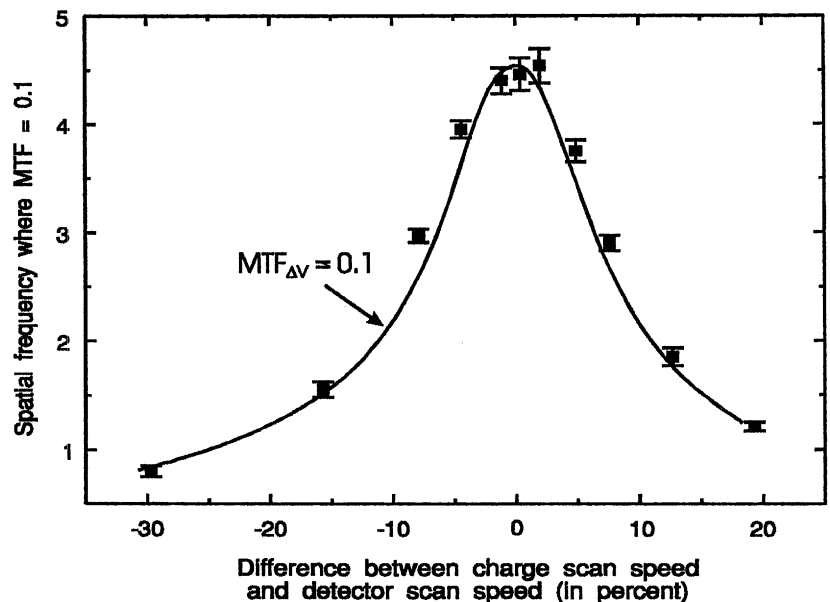


**Figure 8** Comparison of the measured and calculated effect of mismatch between the scan speed of the detector and the CCD clock frequency.

The total measured NPS,  $W_T(f)$ , are shown after binning (averaging) values from adjacent frequencies. The spectral values of groups of 16 adjacent frequencies in the original spectrum were binned to generate the spectra presented. The zero frequency values of the measured spectra are equal to zero because fluctuations were calculated about the mean signal. Hence the lowest frequency spectral value is the average of 15 adjacent values in the original spectra (i.e. the zero spatial-frequency value was not included in the average). The spectral estimates have a standard error of 2.6%.

The total NPS,  $W_T(f)$ , can be expressed as the sum of three uncorrelated constituent noise sources<sup>32</sup>.

$$W_T(f) = W_Q(f) + W_{SQ}(f) + W_D(f) \quad , \quad (7)$$

where  $W_Q(f)$  is the NPS due to x-ray quantum fluctuations,  $W_{SQ}(f)$  is the NPS of the secondary quantum fluctuations, and  $W_D(f)$  is the NPS due to inherent detector output signal fluctuations. It is possible to measure  $W_{SQ}(f)$  and  $W_D(f)$  separately.  $W_{SQ}(f)$  is measured by illuminating the entire detector surface with a uniform light source.  $W_D(f)$  is measured by acquiring images without illumination or x irradiation.  $W_Q(f)$  was calculated by subtracting  $W_D(f)$  and  $W_{SQ}(f)$  from  $W_T(f)$ .

The results of these experiments and calculations are shown for the slot and scan directions in Figures 9-a and 9-b. In the slot direction,  $W_D(f)$  is white and is the dominant noise source at spatial frequencies greater than 3 mm<sup>-1</sup>. In the scan direction,  $W_D(f)$  is the dominant noise source at all spatial frequencies. The shape is similar to the function, 1/f. Added to this inherent detector noise, is the spatial frequency independent secondary quantum noise, and the x-ray quantum noise, which is spatial frequency dependent. The 1/f noise is due to fluctuations in the amplifier reference voltage relative to the CCD bias voltage, and is currently being addressed. Methods of reducing the magnitude of  $W_D(f)$  are also under investigation.

Note that the values of  $W_D(f)$  and  $W_{SQ}(f)$  in the slot direction are equal to the high spatial-frequency values in the scan direction. This occurs because every line in the slot direction is read-out and digitized in a time interval which is shorter than that required to read-out 2 pixels in the scan direction. Therefore, slowly varying temporal-fluctuations in the CCD bias or digitization offset will affect low spatial-frequencies in the scan direction. Rapid temporal-fluctuations will affect high spatial-frequencies in the scan direction, and all spatial-frequencies in the slot direction.

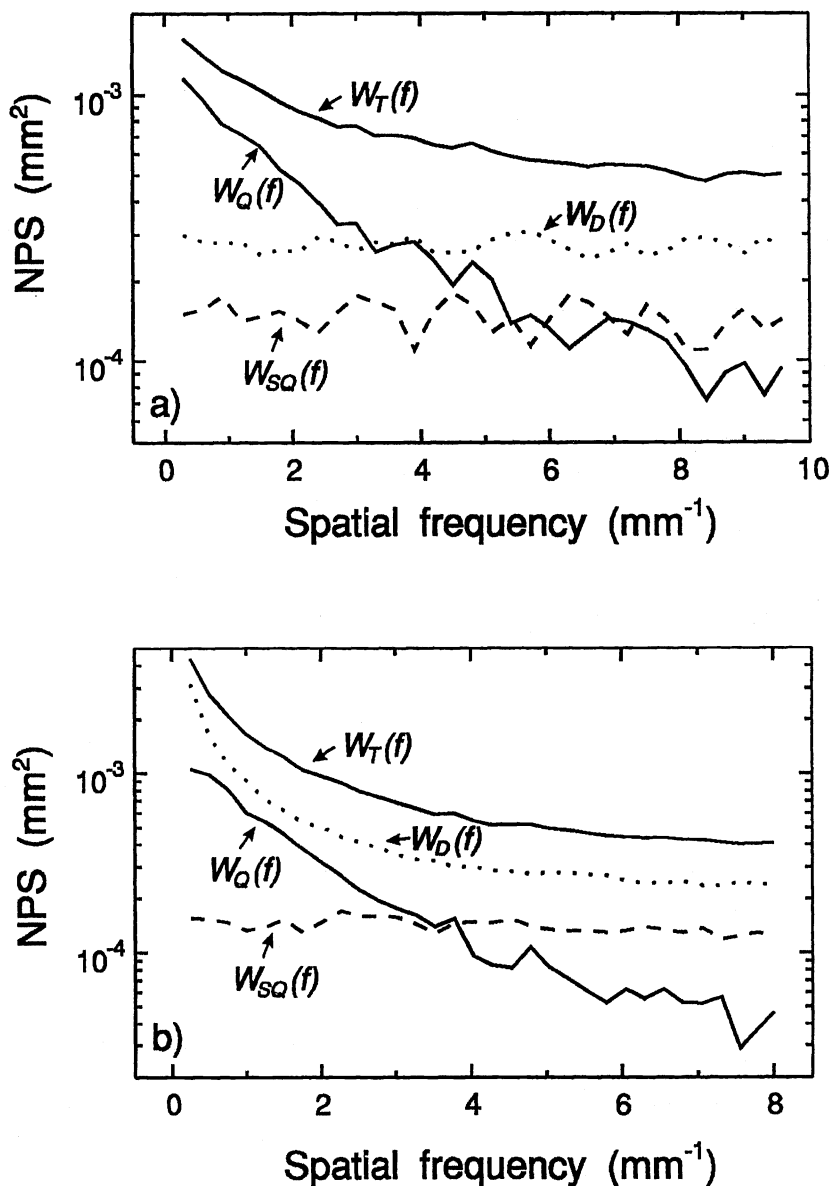


**Figure 9** NPS of the image system in a) the scan and B) the slot direction. The x-ray quantum NPS, secondary quantum NPS and inherent detector NPS are also shown.

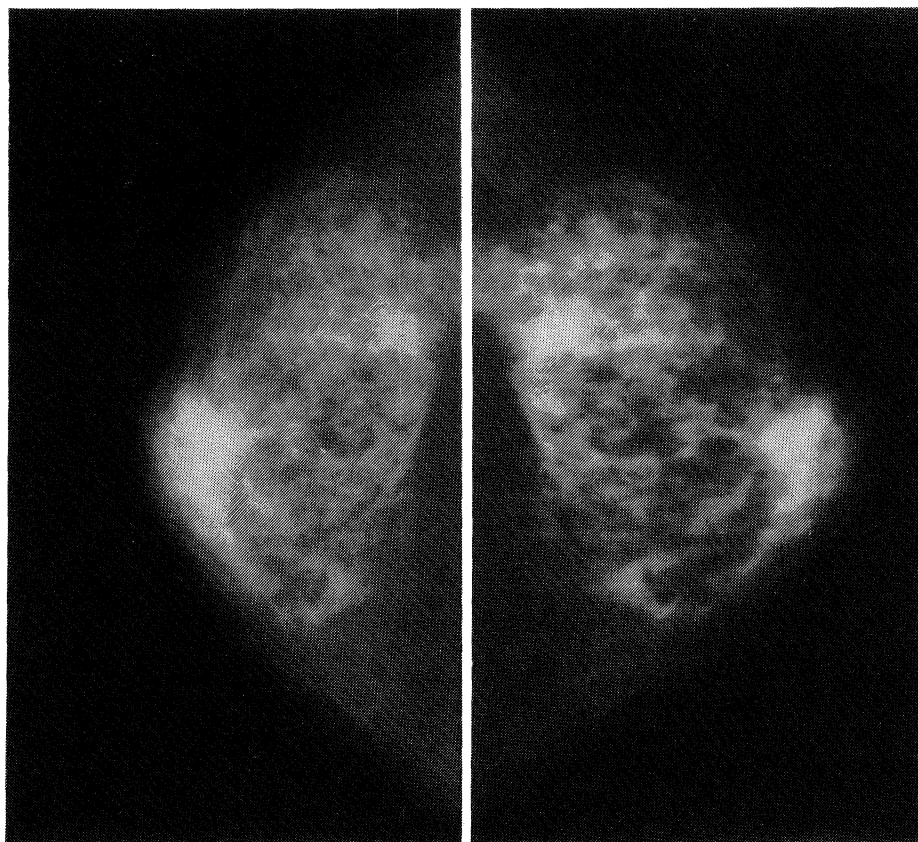


**Figure 10** Images of an anthropomorphic breast phantom. The film image (left) was acquired with a 28 kV Mo-spectrum and a dose of 1.1 mGy. The digital image (right) was acquired with a 40 kV W-spectrum and a dose of 0.85 mGy.

### 3.5. Phantom images

In Figure 10, a digital and a film image of an anthropomorphic phantom are shown. The digital images was acquired with a 40 kV tungsten-target spectrum, while the film image was acquired with a dedicated state-of-the-art mammography system (GE-CGR 600T), Kodak Min-R medium, OM-1 screen-film combination, and a 28 kVp molybdenum-target spectrum with 30  $\mu\text{m}$  molybdenum added filtration. The digital images was acquired with a dose of 0.85 mGy, while the film image was obtained with a dose of 1.1 mGy. We calculated the mean glandular dose assuming a 5 cm thick, 50% adipose, 50% glandular breast<sup>33</sup>. The digital image was displayed with similar contrast to the film image, however, significantly more contrast could have been used to display any region of the breast. The ability to vary display contrast after acquisition is a significant advantage of digital mammography. Notice that the digital image has better resolution near the chest wall than near the nipple. The phantom is designed to be imaged with the focal spot directly above the chest wall. In this preliminary test bench image, the phantom was scanned, hence the focal spot position moved as the phantom moved. The result, as expected, is an apparent unsharpness near the nipple.

In other experiments, we have shown that at least 12 of 16 objects (4 masses, 3 groups of specks, and 5 fibers) are visible in digital images of the ACR accreditation phantom (RMI, Model 156). This exceeds the requirements of the ACR. At a dose of 0.85 mGy, the mean score of 647 mammography imaging systems<sup>34</sup> was 3.3 masses, 2.9 groups of specks, and 4.1 fibers. Thus the digital system performance exceeds the average performance for all three types of objects. In addition, latitude was measured subjectively using a mammographic latitude phantom (RMI, Model 153B). Film-screen images provided adequate contrast to detect objects over a 1.7 cm range of thicknesses of lucite, while the digital detector provided adequate contrast to detect objects throughout the phantom.

#### 4. SUMMARY

A digital mammography imaging system has been developed which is potentially suitable for diagnostic imaging in the clinic. The system has a limiting spatial-resolution of  $9.5 \text{ mm}^{-1}$ . With this system, we have demonstrated the potential of a digital mammography system to acquire images of quality equal to or better than film. The digital system was also better able to image a phantom demonstrating large exposure variations (large latitude) than a state-of-the-art mammographic film-screen system. Currently, images produced with the digital system contain artifacts resulting from the detector noise, which are being addressed. These improvements should increase the value of  $\text{DQE}(f)$  at all spatial frequencies.

For the detector to be x-ray quantum-noise-limited at all spatial frequencies, it is necessary to reduce the magnitude of  $W_D(f)$  and  $W_{SQ}(f)$ . In the mean-variance experiment, we measured a RMS detector noise of  $396 \pm 15 e^-$ . Hguyen, *et al.*<sup>23</sup> have reported that the minimum value of RMS detector noise should be  $40 e^-$ . The detector noise can be significantly reduced by using correlated-double sampling<sup>35</sup>, an AC-coupled amplifier with dark clamp, and cooling the detector to near  $0^\circ \text{C}$ . These modifications will also eliminate the  $1/f$  noise currently seen in the scan direction. If a 10-fold reduction in the RMS noise can be achieved, then the value of  $W_D(f)$  will decrease 100-fold. The value of  $W_{SQ}(f)$  will decrease when the optical coupling is improved. If a 1.0 NA fiber-optic taper is coupled directly to the CCD, then coupling efficiency will increase 5-fold, and  $W_{SQ}(f)$  will decrease relative to  $W_Q(f)$  by a similar amount. With these improvements, the detector will be x-ray quantum-noise-limited at all spatial frequencies.

#### 5. ACKNOWLEDGEMENTS

The authors would like to thank Dr. John Rowlands, N. Robert Bennett, and Roman Lewkow for their help with this project. Equipment has been provided by GE Medical Systems Canada, Kodak Canada, and Varian/Eimac Canada. This work is supported by the Medical Research Council of Canada, and the National Cancer Institute of Canada. The first author is the recipient of a University of Toronto Open Doctoral Fellowship.

#### 6. REFERENCES

1. D.B. Kopans, "Nonmammographic breast imaging techniques: Current status and future developments", *Radiol. Clin. North Am.*, **25**(5), pp. 961-971 (1987).
2. D.B. Kopans, J.E. Meyer, and N. Sadowsky, "Breast Imaging", *New England J. Med.*, **130**(15), pp. 960-967 (April 12, 1984).
3. E.A. Sickles, "Breast imaging: A view from the present to the future", *Diagn. Imag. Clin. Med.*, **54**, pp. 118-125 (1985).
4. R.M. Nishikawa, G.E. Mawdsley, A. Fenster and M.J. Yaffe, "Scanned projection digital mammography", *Med. Phys.*, **17**(5), pp. 717-727 (1987).
5. J.M. Sabol and D.B. Plewes, "Latitude limitations of film-screen mammography", *Med. Phys.*, **18**(5), p. 1076 (1991).
6. P.C. Bunch, K.E. Huff, and R. Van Metter, "Sources of noise in high-resolution screen-film radiography", in R.H. Schneider and S.J. Dwyer III, Eds., *Medicine XIV / PACS IV*, Proc. SPIE, **626**, pp. 64-75 (1986).
7. R.M. Nishikawa and M.J. Yaffe, "Signal-to-noise properties of mammographic film-screen systems", *Med. Phys.*, **12**(1), pp. 32-39 (1985).
8. G.T. Barnes and I.A. Brezovich, "The intensity of scattered radiation in mammography", *Radiology*, **126**(1), pp. 243-247 (1978).
9. D.R. Dance, J. Persliden, and G.A. Carlsson, "Calculation of dose and contrast for two mammographic grids", *Phys. Med. Biol.*, **37**(1), pp. 235-248 (1992).
10. A.D.A. Maidment and M.J. Yaffe, "Scanned-slot digital mammography", in R.H. Schneider, Ed., *Medical Imaging IV: Image Formation*, Proc. SPIE, **1231**, pp. 316-326 (1990).
11. M.J. Yaffe, R.M. Nishikawa, A.D.A. Maidment, and A. Fenster, "Development of a digital mammography system", in R.H. Schneider, and S.J. Dwyer III, Eds., *Medical Imaging II: Part I - Image Formation, Detection, Processing and Interpretation*, Proc. SPIE, **914**, pp. 182-188 (1988).

12. G.T. Barnes, H.M. Cleare, and I.A. Brezovich, "Reduction of scatter in diagnostic radiology by means of a scanning multiple slit assembly", *Radiology*, **120**, pp. 691-694 (1976).
13. M.V. Yester, G.T. Barnes, and M.A. King, "Experimental measurements of the scatter reduction obtained in mammography with a scanning multiple slit assembly", *Med. Phys.*, **8**(2), pp. 158-162 (1981).
14. R. Fahrig, A.D.A. Maidment, and M.J. Yaffe, "Optimization of peak kilovoltage and spectral shape for digital mammography", in R. Shaw, Ed., *Medical Imaging VI: Instrumentation*, Proc. SPIE, **1651**, pp. 74-83 (1992).
15. R. Birch, M. Marshall, and G.M. Ardan, *Catalogue of Spectral Data for Diagnostic X-rays*, HPA Scientific Report Series 30, (Hospital Physicists' Association, 1979), p. 134.
16. A.D.A. Maidment, R. Fahrig, and M.J. Yaffe, "Dynamic range requirements in digital mammography", Submitted for publication to *Medical Physics* (1992).
17. Manufacturer's specifications, RA2048J TDI-CCD image array (EG&G Reticon, Sunnyvale, CA, 1988).
18. R.A. Buchanan, "An improved x-ray intensifying screen", *IEEE Trans. Nucl. Sci.*, **NS-19**(1), pp. 81-86 (1972).
19. E.H. Eberhardt, "Source-detector spectral matching factors", *Appl. Opt.*, **7**(10), pp. 2037-2047 (1968).
20. A.D.A. Maidment and M.J. Yaffe, "Analysis of signal propagation in optically-coupled digital mammography detectors", In preparation for submission to *Medical Physics* (1993).
21. L. Mortara and A. Fowler, "Evaluations of charge-coupled device (CCD) performance for astronomical use", in J.C. Geary, and D.W. Latham, Eds., *Solid State Imagers for Astronomy*, Proc. SPIE, **290**, pp. 28-33 (1981).
22. G.R. Sims and M.B. Denton, "Characterization of a charge-injection-device camera system as a multichannel spectroscopic detector", *Opt. Eng.*, **26**(10), pp. 1008-1019 (1987).
23. B.T. Hguyen, H-F. Tseng, and G.P. Weckler, "A 2048x64 tapped time-delay-and-integration charge-coupled image device", *Proc. SPIE* **972**, pp. 60-64 (1988).
24. D.W. Holdsworth, R.K. Gerson, and A.Fenster, "A time-delay integration charge-coupled device camera for slot-scanned digital radiography", *Med. Phys.*, **17**(5), pp. 876-886 (1990).
25. P.F. Judy, "The line spread function and modulation transfer function of a computed tomographic scanner", *Med. Phys.*, **3**(4), pp. 233-236 (1976).
26. R. Van Metter, *Private communication* (1989).
27. T.S. Lomheim, *et al.*, "Electro-optical hardware considerations in measuring the imaging capability of scanned time-delay-and-integrate charge-coupled imagers", *Opt. Eng.*, **29**(8), pp. 911-927 (1990).
28. M. Tecotzky, *Private communication* (1993).
29. D.F. Barbe, "Time delay and integration image sensors", in *Solid State Imaging*, Proceedings of the NATO Advanced Study Institute on Solid State Imaging (Noordhoff-Leyden, 1976), pp. 659-671.
30. R.F. Wagner, "Fast Fourier digital quantum mottle analysis with application to rare earth intensifying screens", *Med. Phys.*, **4**(2), pp. 157-162 (1977).
31. J.C. Dainty and R. Shaw, *Image Science* (Academic Press, New York, 1974), Chapters 6 and 8.
32. R.M. Nishikawa and M.J. Yaffe, "Effect of various noise sources on the detective quantum efficiency of phosphor screens", *Med. Phys.*, **17**(5), pp. 887-893 (1990).
33. M. Rosenstein, L.W. Anderson, and G.G. Warner, *Handbook of Glandular Tissue Doses in Mammography*, (FDA Publication 85-8239, Rockville, Maryland, 1985).
34. R.E. Hendrick, "Standardization of image quality and radiation dose in mammography", *Radiology*, **174**(3), pp. 648-654 (1990).
35. M.H. White, D.R. Lampe, F.C. Blaha, and I.A. Mack, "Characterization of surface channel CCD image arrays at low light levels", *IEEE J. Solid State Circuits*, **9**(1), pp. 1-13 (1974).